

# Performance Evaluation of High-Power Microwave Systems Against UAVs: A Probabilistic Antenna–Propagation Framework with Sensitivity Analysis

Muhammad Khalil, *Member, IEEE*, Ke Wang, *Senior, IEEE*, and Jinho Choi, *Fellow, IEEE*

**Abstract**—This paper develops an antenna-and-propagation-centric probabilistic framework for quantifying the effectiveness of high-power microwave (HPM) engagements against unmanned aerial vehicles (UAVs). The model couples stochastic UAV kinematics with an antenna/bore sight jitter formulation and atmospheric propagation to obtain closed-form statistics of the received pulse energy, from which both per-pulse and cumulative neutralization probabilities follow. Near-bore sight beam shaping is captured by a jitter-to-gain mapping, slant-range variability arises from integrated acceleration noise, and path loss includes free-space spreading with gaseous and rain attenuation; device susceptibility is represented by a logistic energy-response. Closed-form moments and log-normal closures yield an analytically evaluable per-pulse mean neutralization probability (via Gaussian–Hermite quadrature) and a cumulative dwell-time expression under the standard independence assumption.

Analytical predictions closely match large-scale Monte-Carlo simulations across wide parameter ranges. With a representative commercial threshold of  $E_{\text{th}} = 10^{-2} \text{ J}$ , the model predicts  $\bar{P}_{\text{kill}} \gtrsim 0.4$  per pulse and  $P_{\text{kill,tot}} > 99\%$  within  $\sim 0.1 \text{ s}$  at kHz PRF; for hardened platforms with  $E_{\text{th}} = 10^{-1} \text{ J}$ ,  $\bar{P}_{\text{kill}} < 1\%$  and  $P_{\text{kill,tot}} < 20\%$  after 1 s. A closed-form sensitivity (elasticity) analysis shows that performance is dominated by slant-range ( $S_R \approx -2$ ), with a strong secondary dependence on aperture diameter and transmit power, while pointing jitter and atmospheric variability are comparatively less influential over the evaluated regimes. The resulting antenna/propagation levers provide transparent guidance for HPM system sizing and risk-aware mission planning.

**Index Terms**—Antennas and propagation, pointing jitter, effective antenna gain, atmospheric attenuation, log-normal channels, stochastic kinematics, high-power microwave (HPM), UAV neutralization, Gaussian–Hermite quadrature, sensitivity analysis.

## I. INTRODUCTION

Unmanned aerial vehicles (UAVs), ranging from small commercial quadcopters to advanced defense platforms, have emerged as transformative technologies in modern defense and security operations. The rapid proliferation of UAV technology has significantly reshaped the dynamics of modern warfare, offering versatile and cost-effective tools for state and non-state actors in intelligence gathering, targeted strikes, and electronic warfare [1], [2]. The capability of adversaries to deploy inexpensive drones, often in coordinated swarms, has introduced

The authors Khalil and Wang are with the School of Engineering, RMIT University, Melbourne, Australia. Emails: muhammad.khalil@rmit.edu.au, and ke.wang@rmit.edu.au. The author Choi with the University of Adelaide, Adelaide, Australia. Email: jinho.choi@adelaide.edu.au

significant challenges for traditional defense systems, which struggle to efficiently engage multiple simultaneous threats [3], [4]. This tactical asymmetry was vividly demonstrated in recent conflicts, where low-cost UAV forced defenders to expend disproportionately costly resources on interception measures, thereby highlighting the widening economic disparity in UAV-based warfare. Despite extensive research efforts and substantial defense investments, current counter-UAV (C-UAV) technologies exhibit critical limitations. Kinetic solutions, including artillery and missile interceptors, are effective against isolated drone threats but rapidly become unsustainable in swarm scenarios due to limited ammunition, high operational costs, and significant risks of collateral damage [4]. Direct energy solutions, such as high-energy lasers, offer precise targeting capabilities; however, their operational effectiveness is strongly constrained by atmospheric conditions, environmental interference, and line-of-sight requirements [5]. Moreover, both kinetic and laser-based systems inherently engage targets sequentially, limiting their scalability against coordinated swarms [6]. Non-kinetic methods, including radio-frequency jamming and spoofing, are increasingly challenged by UAVs equipped with autonomous navigation and robust anti-jamming countermeasures [7].

In response to these challenges, high-power microwave (HPM) technology has emerged as a promising approach for countering UAV. HPM weapons deliver concentrated bursts of electromagnetic energy capable of coupling directly into UAV's electronic systems, effectively disrupting or destroying their internal components [8]. Unlike conventional methods that rely on kinetic impact or thermal destruction, HPM weapons neutralize UAV electronics through rapid and non-kinetic mechanisms, significantly reducing the risk of collateral damage [9]. A critical operational advantage of HPM systems is their speed-of-light engagement capability, which allows for near-instantaneous energy delivery to targets once they are within the weapon's operational beam range [8]. Additionally, the reliance of HPM systems on electrical energy rather than expendable munitions ensures an effectively unlimited operating magazine, subject only to the available power and cooling constraints. This circumstance provides a substantial economic advantage over conventional munitions [10]. Furthermore, the ability of HPM systems to produce broad-area effects by adjusting antenna configurations and pulse parameters facilitates the simultaneous neutralization of

multiple UAV threats, significantly improving their suitability against swarm tactics [11].

Real-world demonstrations by programs such as the United States Air Force Research Laboratory's Tactical High-Power Microwave Operational Responder (THOR) and Raytheon's PHASER have validated the practical feasibility and operational effectiveness of HPM systems against drone swarms [12], [13]. Despite their promising capabilities, the effective implementation of HPM systems requires overcoming several intricate technical challenges [14]. These include uncertainties related to dynamic beam pointing errors, atmospheric attenuation effects due to humidity and precipitation, and significant variability in UAV electronic susceptibilities resulting from differences in shielding, internal layout, and manufacturing quality [15]. Indeed, experimental findings consistently reveal substantial variations in UAV responses to HPM exposure, underscoring the inherent stochastic nature of HPM-UAV interactions [16]. Consequently, deterministic modeling approaches that ignore or overly simplify these uncertainties are inadequate for reliable operational planning and performance assessment.

This paper addresses these challenges by developing a comprehensive probabilistic engagement framework for neutralizing UAV threats with HPM systems. We model the target UAV as a continuous-time stochastic process that captures both nominal flight and rapid evasive maneuvers. The position-velocity state evolves with bounded, random accelerations, which lead to time-varying but statistically predictable slant-range behavior and enable accurate moment matching for received energy. This kinematic layer is coupled to (i) a statistically averaged beam-steering model that accounts for pointing jitter and aperture-limited gain, (ii) a propagation model that blends free-space spreading with randomized atmospheric attenuation representative of operational conditions, and (iii) a hardware-response model that maps received pulse energy to neutralization probability using a calibrated susceptibility curve. In contrast to deterministic or idealized treatments, this unified formulation explicitly represents operational uncertainty while preserving the key nonlinearities of real engagements.

Within this framework, we derive closed-form expressions for the moments of the received energy and evaluate the mean per-pulse neutralization probability via efficient Gaussian-Hermite quadrature, yielding fast yet accurate predictions. We then extend the analysis to the cumulative neutralization probability over a dwell, assuming pulse independence (i.e., the PRF is large compared to the correlation times of range and pointing). This extension makes the trade-offs explicit among transmit power, aperture size, pulse width/repetition rate, engagement range, atmospheric variability, and pointing stability. Finally, we perform a normalized sensitivity (elasticity) analysis that identifies the parameters exerting the greatest influence on performance, thereby informing robust system sizing and mission planning. To maintain practical relevance, the models are parameterized using publicly available specifications of contemporary HPM platforms (e.g., THOR, CHAMP, PHASER), ensuring that the probabilistic insights map directly to realistic design and operational settings. To

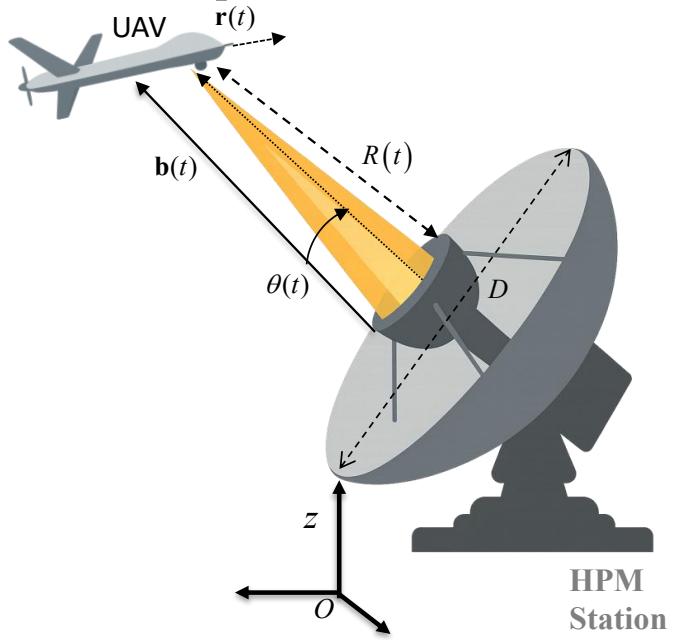


Fig. 1: Engagement geometry between the HPM station and the UAV.

the best of the authors' knowledge, this is the first unified probabilistic HPM-UAV framework that provides closed-form energy and neutralization statistics and validates them against large-scale Monte-Carlo simulations.

The remainder of this paper is organized as follows. Section II develops the stochastic engagement model, covering UAV kinematics, pointing-jitter statistics, propagation, and the energy-to-neutralization mapping. It also derives closed-form expressions for received energy moments, as well as the per-pulse and cumulative neutralization probabilities. Section III presents the sensitivity (elasticity) analysis and discusses the resulting design trade-offs. Section IV provides numerical validations and case studies parameterized by contemporary HPM systems. Section V concludes with key findings and implications for system design and operational planning.

## II. SYSTEM MODEL

The system configuration considered in this study is defined in a Cartesian coordinate system of local geodetic right-hand  $\mathcal{F}_0 = \{O, x, y, z\}$ , where the origin  $O$  corresponds to the location of HPM. The  $x$  axis points north, the  $y$ -axis points east, and the  $z$ -axis aligns with the local vertical direction. The phase center of the transmitting aperture is located at the origin, and its initial boresight is aligned with the  $x$ -axis. Electronic beam steering dynamically directs the main lobe of the antenna pattern toward the target. The elevation of the HPM station above mean sea level is assumed to be negligible relative to engagement ranges, allowing its effect to be omitted in both channel modeling and geometric calculations.

### A. UAV Kinematics and Statistical Modeling of Range

The UAV's movement is represented by a continuous-time stochastic process that captures both nominal flight behav-

ior and rapid evasive maneuvers. At time  $t \in [0, T]$ , the UAV state is described by a six-dimensional vector  $\mathbf{s}(t) = [\mathbf{r}(t)^\top \ \mathbf{v}(t)^\top]^\top \in \mathbb{R}^6$ , where  $\mathbf{r}(t) = [x(t) \ y(t) \ z(t)]^\top$  represents the position and  $\mathbf{v}(t) = \dot{\mathbf{r}}(t)$  denotes the velocity. The time dynamics follow a linear stochastic differential equation,

$$\dot{\mathbf{s}}(t) = \mathbf{F}\mathbf{s}(t) + \mathbf{w}(t) \in \mathbb{R}^6, \quad (1)$$

where  $\mathbf{F}$  represents the linear kinematic relationship between position and velocity, which is explicitly given by

$$\mathbf{F} = \begin{bmatrix} \mathbf{0}_3 & \mathbf{I}_3 \\ \mathbf{0}_3 & \mathbf{0}_3 \end{bmatrix}, \quad (2)$$

where  $\mathbf{0}_n$  and  $\mathbf{I}_n$  denote the  $n \times n$  zero matrix and the identity matrix, respectively. This structure ensures that the time derivative of position yields the instantaneous velocity. On the other hand, acceleration is treated as a random process modeled by a white Gaussian process  $\mathbf{w}(t) \sim \mathcal{N}(0, \mathbf{Q})$  with covariance

$$\mathbb{E}[\mathbf{w}(t) \mathbf{w}^\top(\tau)] = \mathbf{Q} \delta(t - \tau), \quad \mathbf{Q} = \text{diag}(\mathbf{0}_3, \sigma_a^2 \mathbf{I}_3), \quad (3)$$

where  $\delta(\cdot)$  is the Dirac delta function, and  $\sigma_a^2$  is the one-sided power spectral density of the random acceleration, which represents turbulence and evasive maneuvers. This modeling framework ensures that only the acceleration components of the state vector are affected by process noise, accurately reflecting the physical sources of uncertainty in UAV dynamics.

By integrating the linear stochastic differential equation (1) with the initial condition  $\mathbf{s}(0) = [\mathbf{r}_0^\top \ \mathbf{v}_0^\top]^\top \in \mathbb{R}^6$ , we obtain expressions for the mean and covariance of the position vector at time  $t$ . The mean position vector is

$$\bar{\mathbf{r}}(t) = \mathbb{E}[\mathbf{r}(t)] = \mathbf{r}_0 + \mathbf{v}_0 t, \quad (4)$$

where  $\mathbf{r}_0$ , and  $\mathbf{v}_0$ , are the UAV's initial position and velocity, respectively.

The associated position covariance due to integrated acceleration noise is

$$\mathbf{P}_{rr}(t) = \text{Cov}[\mathbf{r}(t)] = \frac{\sigma_a^2 t^3}{3} \mathbf{I}_3, \quad (5)$$

where the factor  $\frac{\sigma_a^2 t^3}{3}$  arises from the integrated effect of white acceleration noise over time. This expression quantifies the growth of uncertainty in each spatial direction due to stochastic accelerations, particularly when the acceleration noise is isotropic (for a general acceleration covariance  $\Sigma_a$ , we have  $\mathbf{P}_{rr}(t) = \frac{t^3}{3} \Sigma_a$ ).

Let the instantaneous slant range between the HPM station and the UAV be a random scalar

$$R(t) \approx \|\mathbf{r}(t)\| = \sqrt{x^2(t) + y^2(t) + z^2(t)}, \quad (6)$$

Under the isotropic model  $\mathbf{P}_{rr}(t) = \sigma_a^2 t^3$ , with  $\sigma_r = \frac{\sigma_a^2 t^3}{3}$ , the vector  $\mathbf{r}(t)$  is Gaussian, with a mean  $\bar{\mathbf{r}}(t)$  and a covariance  $\sigma_r^2(t) \mathbf{I}_3$ . The norm  $R(t)$  follows a non-central chi distribution with  $k = 3$  degrees of freedom and a non-centrality  $\lambda = \frac{\|\bar{\mathbf{r}}(t)\|}{\sigma_r}$ .

Irrespective of isotropy, the second raw moment of the slant range is

$$\mathbb{E}[R^2(t)] = \text{tr}(\mathbf{P}_{rr}(t)) + \|\bar{\mathbf{r}}(t)\|^2. \quad (7)$$

The exact mean  $\mathbb{E}[R^2(t)]$  does not have an elementary closed form in general. A delta-method expansion, valid when the relative spread of  $R(t)$  is modest, yields

$$\bar{R}(t) \equiv \mathbb{E}[R^2(t)] \approx \sqrt{m_2} - \frac{v_2}{8 m_2^{3/2}}, \quad (8)$$

where

$$m_2 = \text{tr}(\mathbf{P}_{rr}(t)) + \|\bar{\mathbf{r}}(t)\|^2, \quad v_2 = \text{tr}(\mathbf{P}_{rr}^2(t)) + 4\bar{\mathbf{r}}^\top \mathbf{P}_{rr} \bar{\mathbf{r}}$$

where  $\text{tr}(\cdot)$  denotes the matrix trace and  $\|\cdot\|$  denotes the Euclidean norm;  $\bar{\mathbf{r}}(t)$  is the deterministic mean trajectory, and  $\mathbf{P}_{rr}(t)$  quantifies the positional uncertainty induced by stochastic accelerations.

From the same expansion, the range variance is approximated by

$$\sigma_R^2(t) = \frac{v_2}{4 m_2}, \quad (9)$$

For subsequent channel calculations, it is convenient to approximate  $R(t)$  as a log-normal random variable when the coefficient of variation is small. Define

$$C_R^2(t) = \frac{\sigma^2(t)}{\bar{R}^2(t)}. \quad (10)$$

When  $C_R^2(t) \lesssim 0.2$ , we adopt the approximation  $\ln R(t) \sim \mathcal{N}(\mu_{\ln R}, \sigma_{\ln R}^2)$  with moment-matched parameters

$$\mu_{\ln R} = \ln \bar{R} - \frac{1}{2} \ln \left(1 + C_R^2\right) \quad \sigma_{\ln R}^2 = \ln \left(1 + C_R^2\right) \quad (11)$$

This approximation preserves the first two moments of the slant range and substantially simplifies the ensuing stochastic channel modeling and performance analysis. In particular, it captures both the mean and the spread of the time-varying propagation path length between the transmitter and the UAV, thereby providing a rigorous basis for risk-aware channel characterization and engagement-probability calculations.

### B. HPM Transmitter and Beam-Steering Model

The HPM system employs a circular aperture with a diameter of  $D$ , an area of  $A = \frac{\pi D^2}{4}$ , an operating frequency of  $f$ , a wavelength of  $\lambda = c/f$ , and a peak pulse power of  $\mathbf{P}_t$ , located at  $O$ .

The boresight direction  $\hat{\mathbf{b}}(t)$  is continuously updated to track the UAV based on real-time measurements and a closed-loop controller with bandwidth  $f_{trk}$  and latency  $\tau_{trk}$ .

The instantaneous pointing error relative to the true line-of-sight is

$$\theta(t) = \cos^{-1}(\hat{\mathbf{b}}(t) \cdot \hat{\mathbf{r}}(t)), \quad \hat{\mathbf{r}}(t) = \frac{\mathbf{r}(t)}{\|\mathbf{r}(t)\|} \quad (12)$$

This error incorporates tracking noise, latency, servo jitter, and atmospheric distortion and is modeled as a zero-mean Gaussian random process:  $\theta \sim \mathcal{N}(0, \sigma_\theta^2)$ , where  $\sigma_\theta^2$  depends on the tracker performance, UAV speed, and environmental effects.

The far-field power pattern of the aperture near the boresight is approximated by:

$$G(\theta) = G_0 \exp(-k \theta^2), \quad (13)$$

where  $G_0 = \left(\frac{\pi D}{\lambda^2}\right)^2$  is the maximum antenna gain (at bore-sight), and  $k = \frac{4\ln 2}{\theta_{3dB}^2}$  characterizes the beam's sharpness. The 3-dB beamwidth for a uniformly illuminated circular aperture is  $\theta_{3dB} \approx 0.886 \lambda/D$ , with an aperture efficiency of  $\epsilon \in (0, 1]$ .

Averaging over jitter yields the average effective antenna gain  $\bar{G}$ , and its variance as follows:

$$\bar{G} = \mathbb{E}[G(\theta)] = G_0 (1 + 2k \sigma_\theta^2)^{-1/2}, \quad (14)$$

$$\text{Var}[G] = G_0^2 \left[ (1 + 4k \sigma_\theta^2)^{-1/2} - (1 + 2k \sigma_\theta^2)^{-1} \right]. \quad (15)$$

This result reveals a critical trade-off between aperture size  $D$  and pointing accuracy  $\sigma_\theta$ . It highlights that larger antenna sizes, while providing higher potential gain, become ineffective if the pointing jitter variance is not simultaneously reduced. Practically, there are diminishing returns when the aperture size exceeds a critical value  $D_{crit} \approx \frac{0.376\lambda}{\sigma_\theta}$ .

### C. Atmospheric Channel and Attenuation Modeling

The propagation path from the transmitter to the UAV traverses the atmospheric channel, characterized by two distinct media: (i) free space, in which spherical spreading dominates, and (ii) the lower troposphere, where molecular absorption and hydrometeors impose additional attenuation. The free-space path loss obeys the Friis relation

$$\mathcal{L}_{FS}(t) = \left( \frac{4\pi R(t)}{\lambda} \right)^2, \quad (16)$$

where  $R(t)$  is the stochastic slant range derived in Section II-A and  $\lambda = c/f$  is the carrier wavelength. Since  $\ln R(t)$  is approximately Gaussian,  $\ln \mathcal{L}_{FS}(t)$  is also Gaussian, implying that  $\mathcal{L}_{FS}(t)$  is log-normally distributed. Closed-form first and second moments therefore follow directly from the range statistics in (8)-(9) [17].

Atmospheric attenuation (dB  $km^{-1}$ ) includes gaseous absorption  $\gamma_{gas}$  and precipitation  $\gamma_{rain}$ . Using ITU-R recommendations [18] the total atmospheric attenuation is

$$A_{atm}(f, t) = \underbrace{\gamma_{gas}(f, p, T, \epsilon) \frac{R(t)}{1000}}_{\text{molecular O}_2 + \text{H}_2\text{O loss}} + \underbrace{\gamma_{rain}(f, R_{rain}) \frac{R_{eff}(t)}{1000}}_{\text{precipitation, ITU-R P.838}}, \quad (17)$$

where  $p$  is the total pressure,  $T$  is the absolute temperature,  $\epsilon$  is the water-vapor partial pressure, and  $R_{eff}(t) = R(t) \cos \varphi(t)$  is the effective rain path at the elevation angle  $\varphi(t)$ .

To capture day-to-day and intra-storm variability, the instantaneous rain-rate can be modeled as a Gamma random variable

$$R_{rain}(t) \sim \text{Gamma}(\alpha_r, \beta_r), \quad (18)$$

whose shape  $\alpha_r$  and inverse-scale  $\beta_r$  are obtained from long-term local meteorological records [19], [20]. Under this assumption,  $\gamma_{rain} = k(f) R_{rain}^{\alpha(f)}$  has a mean and variance

$$\begin{aligned} \mathbb{E}[\gamma_{rain}] &= k(f) \frac{\Gamma(\alpha_r + \alpha(f))}{\beta_r^{\alpha(f)} \Gamma(\alpha_r)} \\ \text{Var}[\gamma_{rain}] &= k(f)^2 \left[ \frac{\Gamma(\alpha_r + 2\alpha(f))}{\beta_r^{\alpha(f)} \Gamma(\alpha_r)} - \left( \frac{\Gamma(\alpha_r + \alpha(f))}{\beta_r^{\alpha(f)} \Gamma(\alpha_r)} \right)^2 \right], \end{aligned} \quad (19)$$

where  $k(f)$  and  $\alpha(f)$  are the frequency-dependent coefficients, and  $\psi^{(1)}(\cdot)$  is the trigamma function. Because  $\gamma_{gas}$  is quasi-deterministic on short time-scales, the composite loss  $A_{atm}$  is well approximated by a shifted log-normal random variable. Consequently, the dB expectation and variance of the total attenuation, assuming the independence of  $R$  and  $\gamma_{rain}$ , are

$$\mu_A = [\gamma_{gas} + \mathbb{E}[\gamma_{rain}] \cos \bar{\varphi}] \frac{\bar{R}}{1000}, \quad (20)$$

$$\sigma_A^2 = \gamma_{gas}^2 \left( \frac{\sigma_R}{1000} \right)^2 + (\cos \bar{\varphi} \mathbb{E}[\gamma_{rain}])^2 \sigma_R^2 + \left( \frac{\bar{R} \cos \bar{\varphi}}{1000} \right)^2 \quad (21)$$

$$\text{Var}[\gamma_{rain}] + 2\gamma_{gas} \mathbb{E}[\gamma_{rain}] \cos \bar{\varphi} \left( \frac{\sigma_R}{1000} \right)^2 \quad (22)$$

where  $\bar{R}$  is the slant range in meters,  $\gamma_{gas}$ ,  $\gamma_{rain}$  in dB/km, and  $\bar{\varphi} = \sin^{-1}(\bar{z}/\bar{R})$  is the elevation angle. The factor of 1000 converts the slant range from meters to kilometers to match the ITU-R attenuation unit in dB/km [20]–[22].

Equations (17)–(21) yield closed-form expressions for the moments of attenuation, which can be incorporated directly into the subsequent energy and kill-probability calculations. This approach eliminates the need for computationally intensive Monte-Carlo weather realizations while retaining statistical accuracy and fidelity.

### D. Received Energy and Statistical Neutralization Metric

During an engagement, the HPM transmitter illuminates the target for a dwell time of  $T > 0$  [s]. It emits identical rectangular pulses of peak envelope power  $P_t$  [W] and duration  $\tau_p$  [s] at a pulse-repetition frequency  $f_{PRF}$  [s<sup>-1</sup>]. The number of pulses within the dwell is

$$N = f_{PRF} T. \quad (23)$$

and, by design,  $\tau_p \ll 1/f_{PRF}$ , the duty cycle  $\delta = \tau_p f_{PRF}$  remains small, ensuring thermal feasibility.

The power incident on the UAV electronics is calculated using an adapted Friis equation. Let  $R(t)$  denote the slant range,  $\bar{G}$  the average antenna gain—including pointing jitter—and  $A_{atm}(f, t)$  the atmospheric attenuation in dB. The instantaneous received power during a pulse is described by a Friis-type relation that includes atmospheric loss

$$P_r(t) = P_t \bar{G} \left( \frac{\lambda}{4\pi R(t)} \right)^2 10^{-A_{atm}(f, t)/10} \quad 0 \leq t \leq T,$$

and the energy delivered in one pulse is

$$E_r(t) = P_r(t) \tau_p, \quad (24)$$

For analysis, it is convenient to take logarithms. Collecting deterministic terms and separating the random terms due to pointing, range, and atmosphere yields:

$$\begin{aligned} \ln E_r(t) &= \underbrace{\ln P_t + \ln \tau_p - 2 \ln \left( \frac{4\pi}{\lambda} \right)}_{\text{deterministic}} \\ &+ \underbrace{\ln \bar{G} - 2 \ln \mathbf{R}(t) - \frac{\ln 10}{10} A_{\text{atm}}(f, t)}_{\text{pointing}}. \end{aligned} \quad (25)$$

Under the small-spread approximations established earlier, we model  $\ln \bar{G} \sim \mathcal{N}(\mu_{\ln \bar{G}}, \sigma_{\ln \bar{G}}^2)$ ,  $\ln \mathbf{R}(t) \sim \mathcal{N}(\mu_{\ln R}, \sigma_{\ln R}^2)$ , and  $A_{\text{atm}}(f, t) \sim \mathcal{N}(\mu_A, \sigma_A^2)$ . Consequently, the per-pulse energy is log-normally distributed as follows:

$$\ln E_r(t) \sim \mathcal{N}(\mu_{\ln E}, \sigma_{\ln E}^2), \quad (26)$$

with

$$\mu_{\ln E_r} = \ln(P_t \tau_p) - 2 \ln\left(\frac{4\pi}{\lambda}\right) + \mu_{\ln \bar{G}} - 2 \mu_{\ln R} - \frac{\ln 10}{10} \mu_A, \quad (27)$$

$$\sigma_{\ln E_r}^2 = \sigma_{\ln \bar{G}}^2 + 4 \sigma_{\ln R}^2 + \left(\frac{\ln 10}{10}\right)^2 \sigma_A^2 \quad (28)$$

Here, the parameters  $(\mu_{\ln \bar{G}}, \sigma_{\ln \bar{G}}^2)$  and  $(\mu_{\ln R}, \sigma_{\ln R}^2)$  are computed from the above relative equations as follows.

$$\mu_{\ln \bar{G}} = \ln G_0 - \frac{1}{2} \ln(1+2k\sigma_\theta^2), \quad \sigma_{\ln \bar{G}}^2 = \ln(1+2k\sigma_\theta^2) \quad (29)$$

Experimental studies in [23] have shown that UAV electronics, particularly flight control units and onboard sensors, can suffer functional disruption or permanent damage when exposed to high-power microwave pulses delivering energy levels above a critical threshold. For commercial off-the-shelf (COTS) UAVs, this damage threshold is typically on the order of  $E_{th} \approx 10^{-2}$  J. However, military-grade or hardened UAVs often exhibit significantly higher tolerance due to shielding, surge protection, and redundancy in their electronic subsystems. In this work, we consider  $E_{th}$  as a tunable design parameter to account for different classes of UAV threats, ranging from  $10^{-2}$  J (e.g., toy drones) to 1 J for the worst-case hardened systems.

To capture the probabilistic nature of target susceptibility due to manufacturing variance, shielding quality, or angle of incidence, we model the neutralization (kill) probability using a sigmoid (logistic) function of the received pulse energy  $E$ :

$$P_{\text{kill}}(E_r) = \frac{1}{1 + e^{-\alpha_\kappa(E_r - E_{th})}}, \quad \alpha_\kappa > 0, \quad (30)$$

where  $\alpha_\kappa$  is the kill-probability sigmoid parameter that controls the slope (sharpness) of the transition. This function reflects the fact that small deviations around the threshold  $E_{th}$  can produce widely different outcomes, depending on the drone's internal hardware resilience and system uncertainties.

The mean per-pulse neutralization probability is obtained by averaging the logistic device-response over the log-energy distribution of a single pulse. Let  $x = \ln E_r$  denote the natural logarithm of the received pulse energy; under the small-spread

approximations developed earlier, we take  $x \sim \mathcal{N}(\mu_E, \sigma_{\ln E}^2)$ . The mean per-pulse neutralization probability is therefore

$$\bar{P}_{\text{kill}} = \frac{1}{\sigma_{\ln E_r} \sqrt{2\pi}} \int_{-\infty}^{\infty} \frac{\exp\left[-(x - \mu_{\ln E})^2 / 2\sigma_{\ln E_r}^2\right]}{1 + e^{-\alpha_\kappa(e^x - E_{th})}} dx, \quad (31)$$

where  $\alpha_\kappa > 0$  controls the slope of the logistic transition, and  $E_{th}$  represents the disruption threshold.

The integral in (31) does not admit an elementary closed form but can be evaluated accurately and efficiently using Gauss–Hermite (GH) quadrature. Using the affine change of variables,

$$x = \mu_{\ln E} + \sqrt{2} \sigma_{\ln E} z, \quad (32)$$

and denoting by  $\{(z_i, w_i)\}_{i=1}^n$  the nodes and weights of the  $n$ -point GH rule, we obtain the approximation

$$\bar{P}_{\text{kill}} \approx \frac{1}{\sqrt{\pi}} \sum_{i=1}^n w_i \frac{1}{1 + \exp\left[-\alpha_\kappa\left(\exp(\mu_{\ln E} + \sqrt{2} \sigma_{\ln E} z_i) - E_{th}\right)\right]}. \quad (33)$$

In the parameter ranges of interest, taking  $n = 10$  yields numerical errors well below  $10^{-2}$ , while larger values of  $n$  provide essentially indistinguishable results at a higher computational cost.

Under the standard independence assumption, namely that the pulse–repetition frequency is sufficiently high relative to the correlation times of pointing and range fluctuations, the cumulative neutralization probability after a dwell  $T$  containing  $N = f_{\text{PRF}} T$  pulses is

$$P_{\text{kill,tot}}(T) = 1 - (1 - \bar{P}_{\text{kill}})^{f_{\text{PRF}} T}, \quad (34)$$

where  $\bar{P}_{\text{kill}}$  is the mean per-pulse neutralization probability defined previously. This expression consolidates the effects of the transmitter and tracking parameters  $\{P_t, D, \sigma_\theta, \tau_p, f_{\text{PRF}}\}$ , the stochastic channel variables  $\{R(t), A_{\text{atm}}(f, t)\}$ , and the device–response parameters  $\{E_{th}, \alpha_\kappa\}$  into a single probabilistic performance metric, thereby enabling direct parametric optimization, trade–off analysis, and sensitivity studies.

### III. SENSITIVITY ANALYSIS OF RECEIVED ENERGY AND SYSTEM PARAMETERS

This section quantifies how variations in the key system and environmental parameters influence the received pulse energy and, consequently, the probability of UAV neutralization. A sensitivity framework has been developed to identify the most influential factors, providing a principled basis for resource allocation and design optimization.

#### A. Received-energy model for sensitivity analysis

As established in Eq. (24), the received energy per pulse,  $E_r(t)$ , is a function of the transmit power, pulse width, antenna gain (including pointing jitter), stochastic range, and

atmospheric attenuation. For sensitivity analysis, we focus on the statistical mean,  $\bar{E}$ , which can be expressed as

$$\bar{E} = \mathbb{E}[E_r(t)] = P_t \tau_p G_0 (1 + 2k \sigma_\theta^2)^{-\frac{1}{2}} \left( \frac{\lambda}{4\pi} \right)^2 \exp \left( -2\mu_{\ln R} + 2\sigma_{\ln R}^2 \right) \exp \left( -\frac{\ln 10}{10} \mu_A + \frac{1}{2} \left( \frac{\ln 10}{10} \right)^2 \sigma_A^2 \right). \quad (35)$$

where  $\sigma_\theta^2$  is the pointing jitter variance,  $(\mu_{\ln R}, \sigma_{\ln R}^2)$  represents the mean and variance of the log-range, respectively, and  $\mu_A$  is the mean atmospheric attenuation in dB. Equation (35) provides the exact expectation whenever attenuation is treated as a random (log-normal) variable; if  $\sigma_A^2 \approx 0$  represents negligible variability, the final exponential reduces to the familiar deterministic factor  $10^{-\mu_A/10}$ .

### B. Normalized Sensitivity Definition

To assess how variations in each parameter propagate to the expected received energy, we introduce the normalized sensitivity coefficient (also known as elasticity), defined as

$$S_\chi = \frac{\partial \ln \bar{E}}{\partial \ln \chi}. \quad (36)$$

Here,  $S_\chi$  quantifies the percentage change in the mean received energy  $\bar{E}$  resulting from a one percent change in the parameter  $\chi$ , where  $\chi$  denotes any relevant system or channel variables, such as transmit power, pulse width, antenna diameter, pointing jitter, mean range, or atmospheric attenuation.

By differentiating the analytical expression for  $\bar{E}$  in (35) with respect to the natural logarithm of each parameter, we obtain the explicit closed-form sensitivities summarized in Table I. For the aperture diameter  $D$  and the pointing-jitter standard deviation  $\sigma_\theta$ , the normalized sensitivities (defined as in (36)) are

$$S_D = 2 - \frac{2k\sigma_\theta^2}{1 + 2k\sigma_\theta^2}, \quad (37)$$

$$S_{\sigma_\theta} = -\frac{2k\sigma_\theta^2}{1 + 2k\sigma_\theta^2}, \quad (38)$$

where all terms retain their definitions from Section III-A. These expressions directly link system design parameters (e.g., aperture diameter  $D$ , transmit power  $P_t$ ) and stochastic effects (pointing jitter, atmospheric variability) to engagement performance.

Table I: Closed-form sensitivities of  $\bar{E}$ .

Sensitivity	Value
$S_{P_t}$	1
$S_{\tau_p}$	1
$S_{\bar{R}}$	-2
$S_{\mu_A}$	$-\frac{\ln 10}{10} \approx -0.23$
$S_{\sigma_A^2}$	$\frac{1}{2} \left( \frac{\ln 10}{10} \right)^2 \approx 0.0265$

In particular, the results show that the received energy is consistently linear and sensitive to changes in transmit power and pulse width. The sensitivity to antenna diameter is strongly

Table II: Baseline simulation parameters for HPM–UAV engagement

Parameter	Symbol	Baseline Value
Peak transmit power	$P_t$	200 kW
Pulse width	$\tau_p$	0.5 $\mu$ s
Pulse repetition frequency	$f_{\text{PRF}}$	1 kHz
Carrier frequency	$f$	2.45 GHz (ISM band)
Wavelength	$\lambda$	0.122 m
Antenna diameter	$D$	1.5 m
Pointing jitter (std. dev.)	$\sigma_\theta$	1 mrad
Slant range (nominal)	$\bar{R}$	1 km
Atmospheric attenuation (mean)	$\mu_A$	0.2 dB/km
Damage threshold (baseline UAV)	$E_{\text{th}}$	$10^{-2}$ J
Kill-function slope	$\alpha_k$	50

modulated by pointing jitter. When jitter is negligible, increasing the diameter leads to a quadratic improvement; however, in the jitter-dominated regime, this advantage is lost. Pointing jitter, mean range, and mean atmospheric attenuation all exert negative sensitivities, with range exhibiting the steepest decline due to its inverse-square relationship. The effect of attenuation variability is comparatively minor; however, it is nonetheless included for completeness.

## IV. RESULTS AND DISCUSSIONS

To validate the analytical framework developed in Section II, we conducted both Monte Carlo (MC) simulations and analytical evaluations under a set of baseline assumptions that represent contemporary HPM systems. Unless otherwise specified, the reference scenario uses the parameters listed in Table II. These values are consistent with experimental platforms such as AFRL’s THOR, CHAMP, and Raytheon’s Phaser [23]–[25], which routinely employ peak powers in the 100 kW to MW range and microsecond-scale pulses.

### A. Effect of Damage Threshold on Per-Pulse Neutralization Probability

Fig. 2 shows how the mean per-pulse neutralization probability,  $\bar{P}_{\text{kill}}$ , varies with the damage threshold  $E_{\text{th}}$ . The solid curve represents the theoretical prediction based on the log-normal energy distribution, while the dashed curve shows MC results. It can be seen that analytical predictions closely match Monte Carlo simulations across all thresholds, confirming the accuracy of the log-normal approximation. At low thresholds ( $E_{\text{th}} \sim 10^{-3} - 10^{-2}$  J), representative of lightly shielded commercial UAVs, the neutralization probability remains high and relatively stable, indicating that most pulses deliver enough energy to exceed the disruption criterion. As  $E_{\text{th}}$  increases,  $\bar{P}_{\text{kill}}$  falls steeply, reflecting the diminishing likelihood of a single pulse exceeding the higher damage requirement. For hardened platforms ( $E_{\text{th}} \geq 10^{-1}$  J), the kill probability approaches zero, indicating that individual pulses are ineffective against resilient electronics

### B. Cumulative Neutralization Probability versus Dwell Time

Fig 3 shows the cumulative neutralization probability,  $P_{\text{kill,tot}}$ , as a function of dwell time for several damage thresholds. For each threshold, both theoretical predictions (solid

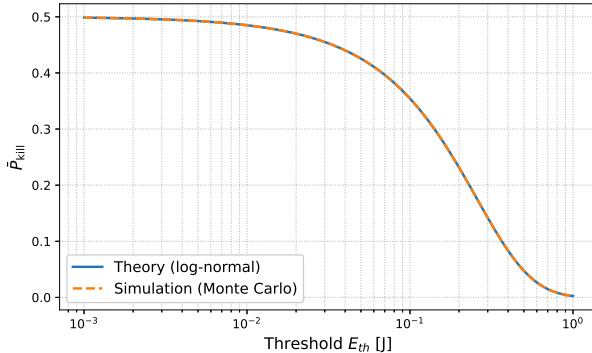


Fig. 2: Mean per-pulse neutralization probability  $\bar{P}_{\text{kill}}$  versus received-energy threshold  $E_{r,\text{th}}$ . Theoretical predictions (solid) are compared with Monte Carlo simulations (markers), showing excellent agreement across thresholds.

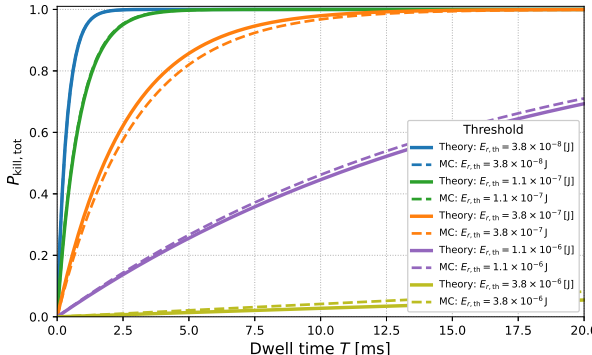


Fig. 3: Cumulative neutralization probability  $P_{\text{kill,tot}}$  versus dwell time  $T$  for several received-energy thresholds  $E_{r,\text{th}}$ . Theoretical predictions (solid) under the log-normal energy model with pulse-independence are compared against Monte Carlo simulations (dashed/markers), showing close agreement. Higher thresholds shift the curves rightward (slower accumulation), whereas vulnerable targets saturate near unity within milliseconds.

lines) and MC results (dashed lines) are plotted. For vulnerable UAVs, cumulative neutralization quickly saturates near unity within milliseconds, confirming the feasibility of rapid engagement. At higher thresholds, the cumulative probability rises more gradually and may remain below 50% even after extended dwell times, illustrating the difficulty of neutralizing hardened or shielded targets. The excellent agreement between analytic and MC results validates the assumption of statistical independence of successive pulses and demonstrates the sensitivity of engagement performance to dwell time and target susceptibility.

#### C. Statistical Distribution of Received Energy

Fig. 4 illustrates the distribution of received pulse energy  $\ln E_r$  under increasing transmit power levels  $P_t$  (from

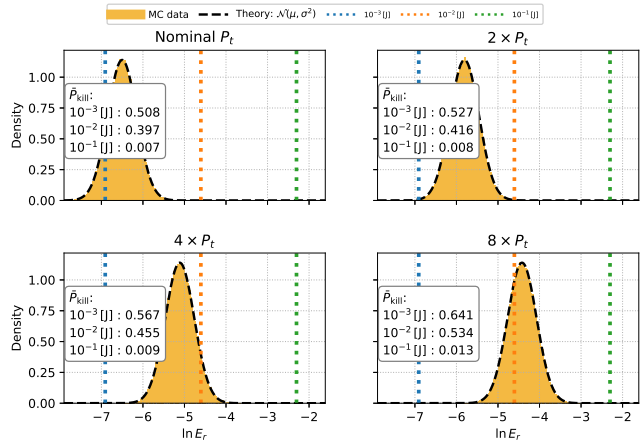


Fig. 4: Effect of increasing  $P_t$  on the distribution of received pulse energy and mean kill probability for log-normal parameters  $\mu_{\ln E_r} = 6.5, E_r = 0.35$  and logistic kill-curve slope  $\alpha_K = 50$ , evaluated for different  $E_{r,\text{th}}$  values.

$P_t$  to  $8P_t$ ). Each subplot overlays an MC-derived histogram with the corresponding log-normal probability density function and marks three representative damage thresholds ( $10^{-3}\text{J}$ ,  $10^{-2}\text{J}$ , and  $10^{-1}\text{J}$ ) on the abscissa. Annotated boxes report the calculated values of  $\bar{P}_{\text{kill}}$  for each threshold using Eq. (31). It is clear from the figure that the log-normal model accurately reproduces the MC-derived histograms. It also shows that increasing  $P_t$  shifts the energy distribution rightward (higher mean energy) while maintaining its log-normal shape, thereby increasing the fraction of pulses that exceed a given threshold. For example, at the baseline power level,  $\bar{P}_{\text{kill}}$  is approximately 0.508, 0.397, and 0.007 for the three thresholds; doubling  $P_t$  increases these values to 0.641, 0.534, and 0.013, respectively. This monotonic trend explains the dwell-time results shown in Fig. 3: higher transmit power increases the per-pulse kill probability, thus reducing the number of pulses (or the time) required to achieve a desired cumulative neutralization probability.

#### D. Neutralization Probability versus Transmit Power

Fig. 5 shows the mean per-pulse kill probability as a function of relative transmit power for three damage thresholds. The abscissa is normalized to a reference transmit power and displayed logarithmically; while the ordinate shows  $\bar{P}_{\text{kill}}$ . All curves exhibit a sigmoidal form, consistent with the logistic kill model in Eq. (31). For low thresholds, modest increases in  $P_t$  rapidly drive  $\bar{P}_{\text{kill}}$  towards unity. In contrast, for hardened targets ( $10^{-1}\text{J}$ ), substantial power increases are required to achieve even a moderate neutralization probability. These results demonstrate the crucial role of transmission power in determining the effectiveness of HPM systems.

#### E. Role of Antenna Diameter

Fig. 6 explores the dependence of  $\bar{P}_{\text{kill}}$  on the antenna diameter  $D$  for three damage thresholds. As expected, increasing  $D$  enhances antenna gain and, thus, the received energy, which leads to higher neutralization probabilities. This

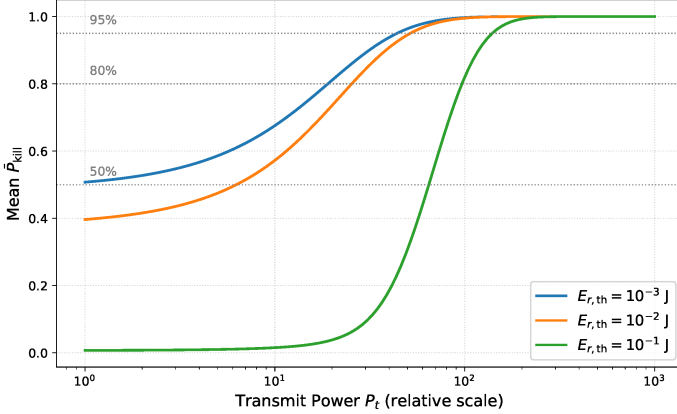


Fig. 5: Mean per-pulse neutralization probability  $\bar{P}_{\text{kill}}$  versus transmit power  $P_t$  for multiple energy thresholds  $E_{\text{th}}$  (theory: solid; MC: markers). Baseline unless noted:  $\tau_p = 0.5 \mu\text{s}$ ,  $f_{\text{PRF}} = 1 \text{ kHz}$ ,  $f = 2.45 \text{ GHz}$  ( $\lambda = 0.122 \text{ m}$ ),  $D = 1.5 \text{ m}$ ,  $R = 1 \text{ km}$ ,  $\sigma_\theta = 1 \text{ mrad}$ ,  $\mu_A = 0.2 \text{ dB/km}$ ,  $\alpha_\kappa = 50$ .

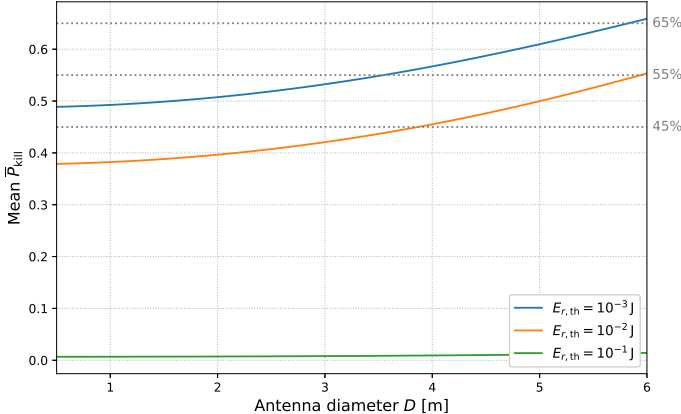


Fig. 6: Mean per-pulse neutralization probability  $\bar{P}_{\text{kill}}$  versus antenna diameter  $D$  for multiple energy thresholds  $E_{\text{th}}$  (theory: solid; MC: markers). The dependence on  $D$  includes both the aperture gain  $G_0 = 4\pi(\pi D^2/4)/\lambda^2$  and the beam-jitter factor  $(1 + 2k\sigma_\theta^2)^{-1/2}$  with  $k = 4 \ln(2)/\theta_{3\text{dB}}^2$  and  $\theta_{3\text{dB}} = 0.886 \lambda/D$ . Baseline unless noted:  $P_t = 200 \text{ kW}$ ,  $\tau_p = 0.5 \mu\text{s}$ ,  $f_{\text{PRF}} = 1 \text{ kHz}$ ,  $f = 2.45 \text{ GHz}$  ( $\lambda = 0.122 \text{ m}$ ),  $R = 1 \text{ km}$ ,  $\sigma_\theta = 1 \text{ mrad}$ ,  $\mu_A = 0.2 \text{ dB/km}$ ,  $\alpha_\kappa = 50$ .

improvement is most pronounced for low thresholds, where a moderate increase in aperture (e.g., from 0.5 m to 2 m) can raise  $\bar{P}_{\text{kill}}$  well above 50 %. For higher thresholds ( $\geq 10^{-1} \text{ J}$ ), however, the probability remains negligibly low across the entire diameter range, highlighting the difficulty of defeating hardened electronics through aperture growth alone. These results demonstrate that antenna scaling is most effective for commercial-grade UAVs; however, it has a limited impact on hardened platforms.

#### F. Dependence on Slant Range

The sensitivity of the per-pulse neutralization probability  $\bar{P}_{\text{kill}}$  to the engagement slant range  $R$  for three damage thresholds is shown in Fig. 7. Across all thresholds,  $\bar{P}_{\text{kill}}$  decreases

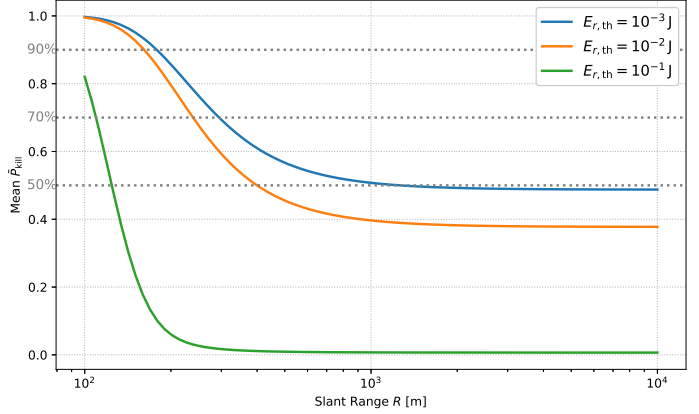


Fig. 7: Mean per-pulse neutralization probability  $\bar{P}_{\text{kill}}$  versus slant range  $R$  for multiple energy thresholds  $E_{\text{th}}$  (theory: solid; MC: markers). The dependence on  $R$  reflects both free-space spreading  $\propto (\lambda/4\pi R)^2$  and atmospheric attenuation  $A_{\text{atm}}(f, R)$ , as modeled in Section II. Baseline unless noted:  $P_t = 200 \text{ kW}$ ,  $\tau_p = 0.5 \mu\text{s}$ ,  $f_{\text{PRF}} = 1 \text{ kHz}$ ,  $f = 2.45 \text{ GHz}$  ( $\lambda = 0.122 \text{ m}$ ),  $D = 1.5 \text{ m}$ ,  $\sigma_\theta = 1 \text{ mrad}$ ,  $\mu_A = 0.2 \text{ dB/km}$ ,  $\alpha_\kappa = 50$ .

approximately as  $R^{-2}$ , which is consistent with free-space path loss. For the most vulnerable targets ( $E_{\text{th}} = 10^{-3} \text{ J}$ ), the kill probability remains above 50 % at approximately one kilometer under the baseline settings; by contrast, for the most resilient targets ( $E_{\text{th}} = 10^{-1} \text{ J}$ ), neutralization becomes essentially negligible beyond a few hundred meters. This behavior highlights the fundamental trade-off between engagement range and target susceptibility, and it has direct implications for system positioning and operational planning.

#### G. Sensitivity Analysis of Mean Received Energy

Fig. 8 summarizes the normalized sensitivities  $S_\chi$  (as defined in (36)) of the mean received energy  $\bar{E}$  with respect to various parameters: transmit power  $P_t$ , pulse width  $\tau_p$ , antenna diameter ( $D$ ), pointing jitter  $\sigma_\theta$ , mean slant range  $\bar{R}$ , mean atmospheric attenuation  $\mu_A$ , and attenuation variance  $\sigma_A^2$ . Analytic sensitivities (blue bars) are compared with finite-difference estimates obtained from MC simulations (red bars). Positive values indicate that increasing the parameter increases  $\bar{E}$ ; while negative values denote the opposite. The results reveal that  $\bar{E}$  is most strongly sensitive to slant range, with  $S_{\bar{R}} \approx -2$ , indicating that a 1% increase in range yields a 2 % decrease in mean energy. Transmit power, pulse width, and antenna diameter each exhibit sensitivities near +1, reflecting their directly proportional influences. In contrast, pointing jitter, mean attenuation, and attenuation variance have relatively small effects under the considered conditions, indicating that improvements in these parameters yield only marginal energy gains. The close agreement between analytic and simulation results across all parameters validates the theoretical sensitivity expressions and provides actionable guidance: for maximal impact on engagement performance, resources should be directed toward reducing range (e.g., by deploying closer interceptors) and increasing aperture size or transmit power, rather than

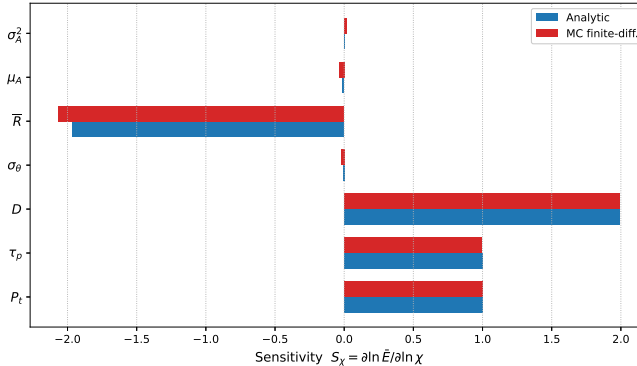


Fig. 8: Normalized sensitivity (elasticity) of mean received energy  $\bar{E}$  with respect to key system and channel parameters,  $S_\chi \triangleq \partial \ln \bar{E} / \partial \ln \chi$ . Bars/curves are evaluated from the analytic model of Section III for  $\chi \in \{P_t, \tau_p, D, \sigma_\theta, \bar{R}, \mu_A, \sigma_A^2\}$  at the baseline operating point. Baseline unless noted:  $P_t = 200$  kW,  $\tau_p = 0.5$   $\mu$ s,  $f_{\text{PRF}} = 1$  kHz,  $f = 2.45$  GHz ( $\lambda = 0.122$  m),  $D = 1.5$  m,  $R = 1$  km,  $\sigma_\theta = 1$  mrad,  $\mu_A = 0.2$  dB/km. For reference, the closed-form elasticities are  $S_{P_t} = S_{\tau_p} = 1$ ,  $S_{\bar{R}} = -2$ ,  $S_{\mu_A} = -\ln(10)/10$ , and  $S_{\sigma_A^2} = \frac{1}{2}(\ln(10)/10)^2$ , while  $S_D$  and  $S_{\sigma_\theta}$  include the beam-jitter coupling through  $k = 4 \ln 2 / \theta_{3\text{dB}}^2$  with  $\theta_{3\text{dB}} = 0.886 \lambda/D$ .

pursuing marginal improvements in jitter or atmospheric compensation.

## V. CONCLUSION

This work presents a unified probabilistic framework for quantifying the effectiveness of HPM engagements against UAVs. The framework integrates (i) stochastic UAV kinematics with closed-form position and range statistics, (ii) a beam-steering model that converts pointing jitter into an effective gain distribution, (iii) an atmospheric channel model with tractable moments for gaseous and precipitation loss, and (iv) a device-response model that maps received pulse energy to the neutralization probability via a logistic transition. A key contribution is the derivation of closed-form moments and log-normal closures that make the received-energy distribution and the associated per-pulse neutralization probability analytically evaluable, substantially reducing reliance on Monte Carlo weather and geometry realizations while preserving statistical fidelity. A second contribution is an explicit sensitivity (elasticity) analysis that yields closed-form expressions for the dependence of the mean received energy on core design and environmental parameters, providing transparent levers for system optimization and mission planning. A third contribution is the end-to-end validation: analytical predictions closely agree with Monte Carlo simulations across a wide parameter range, establishing the accuracy and practical utility of the model.

The results show that neutralization performance is governed by the interplay between target susceptibility and the HPM link budget. The electronic vulnerability of the target, represented by the disruption threshold  $E_{\text{th}}$ , is the dominant factor, followed by transmit power, aperture size (and its interaction with pointing jitter), and engagement range. Consistency

between analysis and simulation confirms the correctness of the received-energy and neutralization-probability models. The closed-form sensitivities clarify why decreasing range or increasing either power or aperture yields the largest gains, whereas incremental improvements in pointing accuracy or atmospheric conditions provide comparatively modest benefits over the evaluated regimes. For commercial or unshielded UAVs, current HPM systems can achieve rapid and reliable neutralization within typical dwell times; for hardened platforms, comparable performance requires materially higher power, larger apertures, and/or longer dwell times; moreover, and the achievable range may be fundamentally limited by propagation and jitter constraints.

Overall, the presented framework constitutes a tractable, validated, and design-oriented analytical tool for HPM-UAV engagements. It systematically transforms stochastic kinematics, beam control dynamics, and atmospheric variability into closed-form performance metrics and sensitivity measures that enable rapid trade-off evaluation, parameter optimization, and risk-aware mission planning. Future research will extend the framework to incorporate time-correlated pulse trains, multi-target interactions, and adaptive scheduling strategies that exploit real-time estimates of range, pointing jitter, and atmospheric conditions.

## REFERENCES

- [1] J. Wang, Y. Liu, and H. Song, "Counter-unmanned aircraft system(s) (c-uas): State of the art, challenges, and future trends," *IEEE Aerospace and Electronic Systems Magazine*, vol. 36, no. 3, pp. 4–29, 2021.
- [2] W. Khawaja, V. Semkin, N. I. Ratyal, Q. H. Yaqoob, J. Gul, and I. Guvenc, "Threats from and countermeasures for unmanned aerial and underwater vehicles," *Sensors*, vol. 22, no. 10, p. 3896, 2022. [Online]. Available: <https://doi.org/10.3390/s22103896>
- [3] H. Shakhatreh, A. H. Sawalmeh, A. Al-Fuqaha, Z. Dou, E. Almaita, I. Khalil, N. S. Othman, A. Khereishah, and M. Guizani, "Unmanned aerial vehicles (uavs): A survey on civil applications and key research challenges," *IEEE Access*, vol. 7, pp. 48 572–48 634, 2019.
- [4] M. Sherman, S. Shao, X. Sun, and J. Zheng, "Counter uav swarms: Challenges, considerations, and future directions in uav warfare," *IEEE Wireless Communications*, vol. 32, no. 1, pp. 190–196, 2025.
- [5] S. Javed, A. Hassan, R. Ahmad, W. Ahmed, R. Ahmed, A. Saadat, and M. Guizani, "State-of-the-art and future research challenges in uav swarms," *IEEE Internet of Things Journal*, vol. 11, no. 11, pp. 19 023–19 045, 2024.
- [6] Newsrael. (2025, May) First operational use of laser weapon on u.s. army vehicle targets. Online report describing deployment of DE M-SHORAD system. [Online]. Available: <https://www.newsrael.com/posts/uubdyxuxjy>
- [7] B. Branco, J. Silvestre Serra Silva, and M. Correia, "Cyber attacks on commercial drones: A review," *IEEE Access*, vol. 13, pp. 9566–9577, 2025.
- [8] J. Benford, "History and future of high power microwaves," *IEEE Transactions on Plasma Science*, vol. 52, no. 4, pp. 1137–1144, 2024.
- [9] Physical Sciences Inc., "High-Power Microwaves: Highlights Lower Cost per Shot and Deep Magazine Enabled by Rechargeable Power," Company website, 2024, accessed: 2025-08-01. [Online]. Available: <https://www.psicorp.com/products/electricity-and-magnetism/high-power-microwaves/>
- [10] M. Backstrom and K. Lovstrand, "Susceptibility of electronic systems to high-power microwaves: summary of test experience," *IEEE Transactions on Electromagnetic Compatibility*, vol. 46, no. 3, pp. 396–403, 2004.
- [11] Y. Wang, L. Ma, and Y. Chen, "Electromagnetic energy coupling path and protection method of uav datalink against broad-spectrum high-power microwave radiation," *Radioengineering*, vol. 31, no. 2, pp. 201–209, Jun. 2022.

- [12] J. Trevithick. Air force set to deploy its counter drone phaser microwave weapon overseas. The War Zone. Available: <https://tinyurl.com/y7s84bq3>.
- [13] Z. Zhang, Y. Zhou, Y. Zhang, and B. Qian, "Investigation on the effects of c-band high-power microwave on unmanned aerial vehicle system," *Journal of Electromagnetic Waves and Applications*, vol. 39, no. 4, pp. 476–489, 2025. [Online]. Available: <https://doi.org/10.1080/09205071.2025.2454400>
- [14] G. Hadley, "Thor hammers drone swarm with high-power microwaves," Air & Space Forces Magazine. Available: <https://tinyurl.com/2p9ee24e>, May 2023, [Online; accessed 2025-08-01].
- [15] C. Han and S. Duan, "Impact of atmospheric parameters on the propagated signal power of millimeter-wave bands based on real measurement data," *IEEE Access*, vol. 7, pp. 113 626–113 641, 2019.
- [16] D. Zhang, X. Zhou, E. Cheng, H. Wan, and Y. Chen, "Investigation on effects of hpm pulse on uav's datalink," *IEEE Transactions on Electromagnetic Compatibility*, vol. 62, no. 3, pp. 829–839, 2020.
- [17] A. Goldsmith, *Wireless Communications*. Cambridge University Press, 2005.
- [18] International Telecommunication Union Radiocommunication Sector (ITU-R), "Characteristics of precipitation for propagation modelling," ITU-R, Geneva, Switzerland, Recommendation P.837-6, Feb. 2012, accessed: 2025-08-01. [Online]. Available: [https://www.itu.int/dms\\_pubrec/itu-r/rec/p/R-REC-P.837-6-201202-S!PDF-E.pdf](https://www.itu.int/dms_pubrec/itu-r/rec/p/R-REC-P.837-6-201202-S!PDF-E.pdf)
- [19] Radiocommunication Sector, International Telecommunication Union, "Characteristics of precipitation for propagation modelling," International Telecommunication Union, Recommendation P.837-7, Jun. 2017. [Online]. Available: <https://www.itu.int/rec/R-REC-P.837-7-201706-I/en>
- [20] ITU Radiocommunication Sector (ITU-R), "Attenuation by atmospheric gases and related effects," [https://www.itu.int/dms\\_pubrec/itu-r/rec/pdf/rec.P676-13-2022](https://www.itu.int/dms_pubrec/itu-r/rec/pdf/rec.P676-13-2022), International Telecommunication Union, Geneva, Switzerland, Recommendation ITU-R P.676-13, Aug. 2022, radiowave Propagation Series (P).
- [21] —, "Specific attenuation model for rain for use in prediction methods," <https://www.itu.int/rec/R-REC-P.838-3-200503-I/en>, International Telecommunication Union, Geneva, Switzerland, Recommendation ITU-R P.838-3, Mar. 2005.
- [22] A. Papoulis and S. U. Pillai, *Probability, random variables, and stochastic processes*, 4th ed. Boston: McGraw-Hill, 2002.
- [23] J. Benford, E. Schamiloglu, J. Stephens, J. A. Swegle, and P. Zhang, *High Power Microwaves*, 4th ed. Boca Raton: CRC Press, 2025, vol. 1.
- [24] Defense Update, "New high power microwave weapons: Raytheon phaser and afrl thor," [https://defense-update.com/20190923\\_hpm.html](https://defense-update.com/20190923_hpm.html), Sep. 2019, [Online; accessed 2024-07-30].
- [25] Air Force Research Laboratory, "Afrl conducts swarm technology demonstration at white sands missile range," <https://www.afrl.af.mil/News/Article-Display/Article/3396995/afrl-conducts-swarm-technology-demonstration-at-white-sands-missile-range/>, 2023, [Online; accessed 2024-07-30].